Semiconductor Lasers: Device Physics and Applications

Academic and Research Staff

Professor Rajeev J. Ram, Dr. Holger Schmidt, Dr. Charles Cox III

Graduate Students

Mathew C. Abraham, Erwin Lau, Harry L. T. Lee, Steven G. Patterson, Kevin P. Pipe, Farhan Rana, Mehmet Yanik, Margaret Wang

1 Introduction

The Semiconductor Laser Group within RLE addresses science and technology questions that arise during the development and application of new device technologies. While the central research thrust is on optoelectronic devices the group's efforts have branched into spintronics, quantum transport and micromagnetics. During the last year the research results from the group have included:

- Demonstration of an enhancement in the modulation bandwidth from 16 GHz to 28 GHz in an injection locked semiconductor laser with a coincident reduction in parasitic chirp.
- Demonstration of room-temperature, continuous-wave operation of the first bipolar cascade laser. This laser demonstrated an internal efficiency of 150% and a measured external modulation efficiency of 99.3%. Continuous-wave lasing was realized up to 80 C.
- Demonstration of continuous-wave lasing from a DFB laser fabricated using precision x-ray lithography and low-temperature crystal overgrowth.
- Demonstration of record high fidelity signal transmission using a multimode vertical cavity surface emitting laser.
- Development of a theory for the modulation and noise in an intersubband laser.
- Design of a semiconductor laser that exploits evaporative cooling of electrons.
- Development of a comprehensive Monte Carlo simulation of spin dephasing in a doped semiconductor. Development of a femtosecond pump-probe experiment and the measurement of the spin relaxation in GaAs.
- Demonstration of interaction effects between nanomagnets in dense magnetic media (60 Gb/in2). Array antiferromagnetism was observed for the first time by magnetic force microscopy.

2 Injection Locking of High Speed DBR Lasers

Sponsor

DARPA

Project Staff

MIT: Harry L. T. Lee, Professor Rajeev J. Ram
KTH: Olle Kjeborn, Richard Schatz

High speed direct modulation of the injection current in a semiconductor laser is an important way to transduce an electrical signal into an optical one, but is limited by wavelength chirp and intrinsic bandwidth of the laser. Combined with fiber dispersion, wavelength chirp limits the useful transmission distance, and high modulation bandwidth is necessary to allow high bit rate data transmission in digital modulation and low signal degradation due to non-linear distortion in

analog modulation. We are investigating how these limitations in direct modulation can be overcome by injection locking and non-uniform feedback in DBR lasers.

Injection locking is accomplished by injecting a strong optical signal into the lasing mode of the slave laser at some frequency detuning from the slave cavity resonance.
The direct modulation dynamics can be dramatically different from the free running laser, depending on the degree of frequency detuning and injected power. Reduction in wavelength chirp occurs because the lasing wavelength becomes locked to the master laser and is less sensitive to variations in the cavity resonance, which instead contributes to bandwidth enhancement. This occurs because the total modal photon density depends on the phase between the master and slave fields, which varies during modulation due to the dependence of index on carrier density. This results in an increased coupling between the carriers and photons, giving an effectively higher differential gain.

Non-uniform feedback is accomplished in DBR lasers by utilzing a DBR with a stopband on the order of, or narrower than the fabry-perot resonance in the active part of the cavity. This allows lasing on the sloped part of the DBR stopband which causes the reflectivity to depend on the lasing frequency, a condition termed detuned loading. This variation adds an additional feedback mechanism which stabilizes the lasing frequency to reduce chirp and effectively increases the differential gain to enhance the modulation bandwidth.

Because of the similarity in the mechanisms involved with injection locking and detuned loading, it is unclear how the two will perform when combined by injection locking a DBR laser. Preliminary measurements using the experimental setup in Fig. 1 indicates bandwidth enhancement beyond the maximum free running bandwidth is possible along with evidence of significant chirp reduction.

Data for two injection locked conditions, using DBR lasers fabricated in the Semiconductor Laboratory at KTH in Sweden, is shown in Figs. 2 and 3. For the –11.8dB injection level, the 3dB bandwidth was enhanced to 28GHz, albeit in a non-ideal way since the low frequency efficiency drops by approximately 10dB and the response appears under damped. It is not clear what implications this would have for large signal digital modulation although the high peak suggests excessive ringing may occur. For this injection level, the chirp reduction is likely to be dominated by the injection locking forcing the laser to lase toward the long wavelength side of the DBR. For the –1.9dB injection level, the change in the 3dB bandwidth from 4.25 to 21GHz is quite dramatic. The relative flatness suggests that minimal signal degradation occurs during transmission through 25km of fiber. This may have important ramifications for long distance directly modulated links.

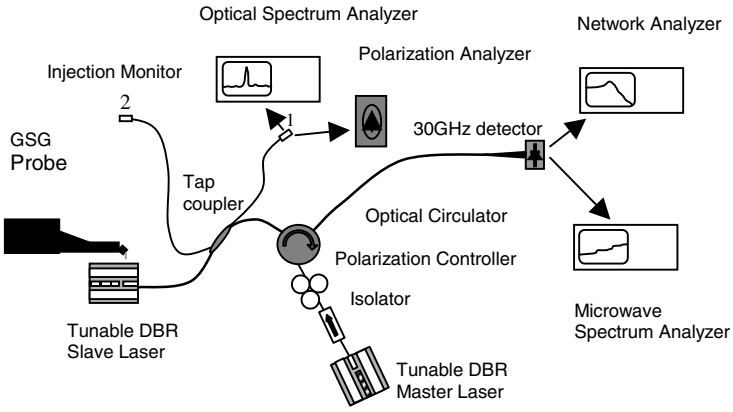

Fig. 1. Experimental setup for optical injection locking DBR lasers. The lasers are mounted on a temperature-controlled stage at 20°C and fiber coupled. The optical circulator allows injection through the front facet of the slave, and provides an additional stage of isolation for the master laser.

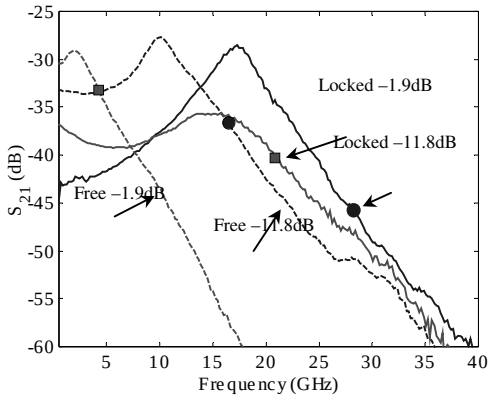

Fig. 2. Modulation response for –11.8dB injection (circles), -1.9dB injection (squares). Solid lines are locked and dashed lines are free running. The solid markers denote 3dB frequency.

3 High Speed DFB Lasers

Sponsor

Defense Advanced Research Projects Agency

Project Staff

MIT: Farhan Rana, Michael H. Lim, Elisabeth Koontz, Professor Leslie Kolodziejski, Professor Henry I. Smith, Professor Rajeev J. Ram

High-speed semiconductor DFB lasers are crucial for high-speed optical communication links. These lasers can be directly modulated at frequencies reaching 20 to 30 GHz. They have important applications in optical links based upon WDM (wavelength division multiplexing) technology. Direct laser modulation schemes are much simpler to implement and integrate than modulation schemes based upon external modulators. However, modulation bandwidth of external modulators can easily go beyond 60 GHz. Thus, it is technologically important to have DFB lasers whose modulation bandwidths compete with those of external modulators. The goal of this project is to develop DFB lasers capable of being modulated at high speeds with low distortion and chirp.

High performance DFB lasers demand that careful attention be paid to the grating design, which provides the optical feedback. Spatial hole burning, side mode suppression, radiation loss, laser linewidth, spontaneous emission in non-lasing modes, lasing wavelength selection and tunability, and laser relaxation oscillation frequency are all features that are very sensitive to the grating design. Improved grating design can significantly enhance laser performance, especially at higher modulation frequencies. Various techniques have been developed that allow fabrication of gratings with spatially varying characteristics and with long-range spatial phase coherence. Using a combination of E-beam, interferometric and X-ray lithographies we can write a variety of

grating patterns. This provides us a unique opportunity for exploring a wide variety of grating designs for semiconductor DFB lasers. We plan to explore laser devices suited for high speed as well as for low noise operation.

We have developed techniques for fabricating high-speed polyimide planarized ridge waveguide laser structures that have low capacitance and are therefore ideally suited for high frequency operation. Fig. 3 shows cross section of a polyimide planarized InP DFB laser. The active region consists of five strain compensated InGaAsP multiple quantum wells. A square grating is imprinted in a InGaAsP layer above the active region by using interferometric and X-ray lithographies. The grating is dry etched with RIE using a mixture of hydrogen and methane gases. A p-doped InP layer is re-grown on top of the grating, followed by a heavily p-doped InGaAs cap layer. The wave-guiding ridges are also formed by dry etching with a hydrogen and methane plasma. Polyimide planarization is achieved by spinning multiple coatings of polyimide followed by a high temperature cure. Cured polyimide is then dry etched with RIE using a mixture of oxygen and carbon tetra-fluoride until the top of the ridge gets exposed. Ohmic contact to the ridge is made by lift-off on top of the polyimide layer. The thick layer of polyimide significantly reduces the capacitance between the top metal contact and the substrate. A large value of this capacitance can short out the active region at high frequencies.

Fig. 4 shows the measured output power from a DFB laser fabricated using the polyimide process. Fig. 5 shows the measured spectrum of the DFB laser. Laser characteristics show good output powers with side mode suppression ratios better than 40 dB.

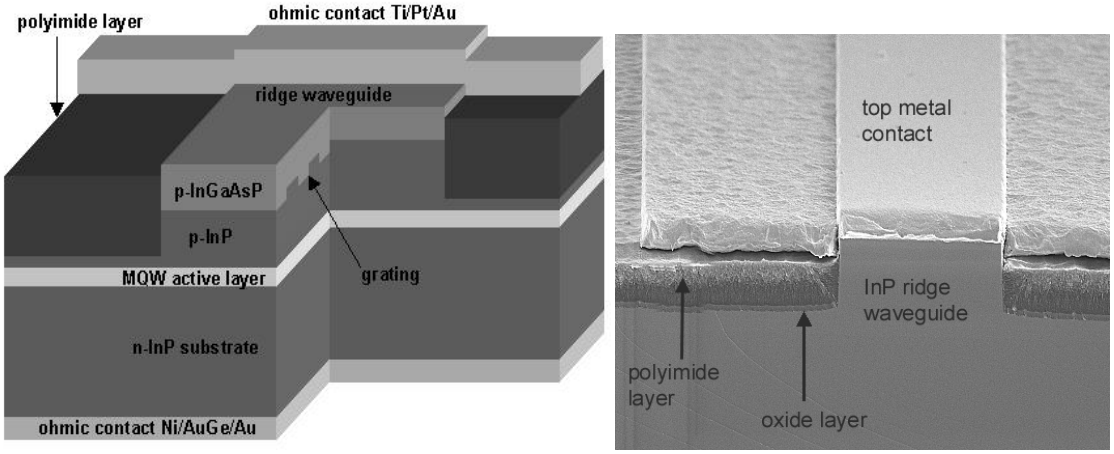

Fig. 3: Polyimide planarized InP DFB ridge-waveguide laser

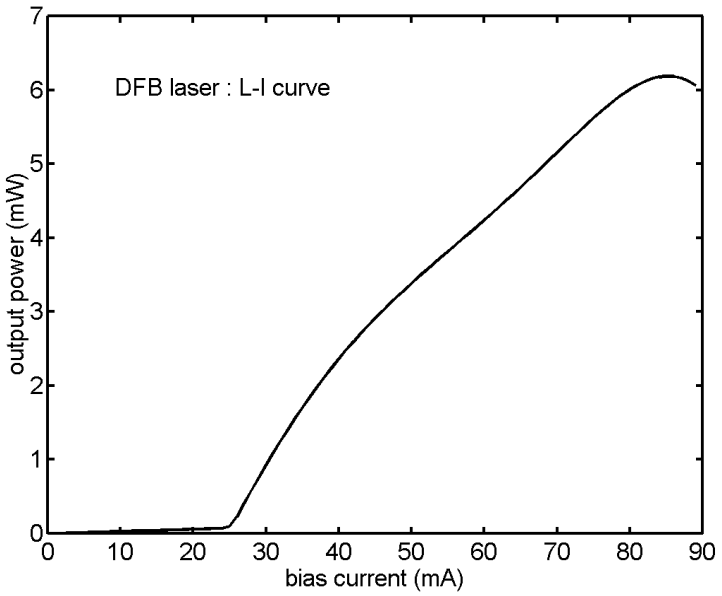

Fig. 4: Measured output power from a DFB laser

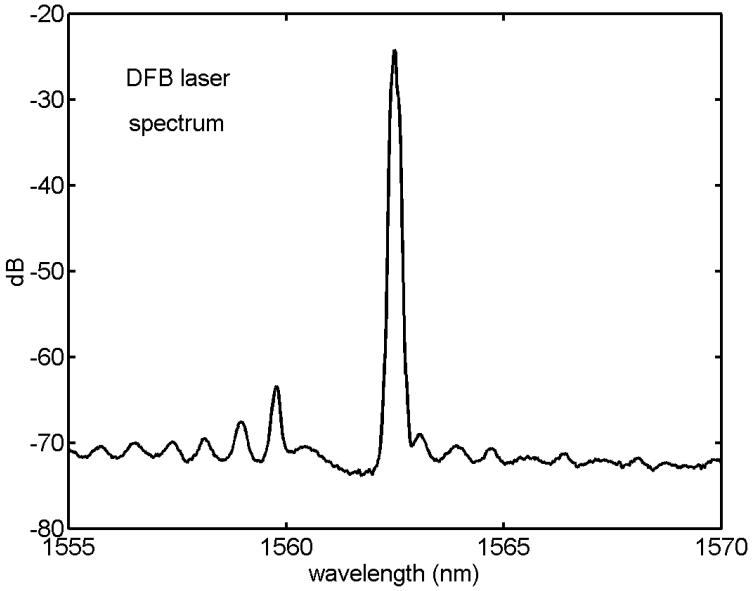

Fig. 5: Measured spectrum of a DFB laser

4 High Fidelity Multimode VCSEL Links

Sponsor

Office of Naval Research

Project Staff

MIT: Harry L. T. Lee, Professor Rajeev J. Ram
Sandia National Labs: Kent Choquette

Using VCSELs for high fidelity RF communication was shown to be feasible for applications requiring modest dynamic range in short multimode links for modulation frequencies that fall within between limits set by mode partition noise and bandwidth of the laser. These issues arise because of the dynamics of the multiple transverse modes in these VCSELs.

While the total optical output of the VCSEL can have low noise, the partitioning of the total power between the different transverse modes fluctuates. When combined with imperfect coupling efficiency into the optical fiber or detector, this results in a much higher noise level than with perfect coupling. This is typically referred to as mode partition noise. The frequency dependence of this noise is important because it sets the lower frequency limit for the useful modulation bandwidth of the VCSEL. In optical link measurements, mode partition noise decreased towards high frequencies but significant mode partition noise degraded performance for frequencies as high as 2-3 GHz.

The effect of multiple transverse modes on the modulation response and non-linear distortions is unclear. Depending on the degree of overlap between the modes and how they share the common carrier density, separate modes may behave like individual lasers, which could limit the modulation bandwidth and increase distortion, or behave as a single laser. Spatial hole burning and carrier diffusion are expected to play a role in the modulation response and non-linear distortion of the VCSELs.

To better understand transverse mode effects, analytical models are being developed to capture multi-transverse mode spatial hole burning effects without resorting to fully spatially varying simulations. Building on previous work that modeled conventional fabry perot lasers, in which the time evolution of the spatial components of the carrier density were followed, convenient 2-D basis function expansions are being developed to allow modeling the spatial evolution of the carrier density and coupling between transverse modes. This level of simplification will allow the development of analytical expressions to estimate the small signal modulation response, distortions, and noise spectral density and provide insight into the physics of the multimode VCSELs.

5 High Efficiency, Bipolar Cascade Lasers

Sponsor

Rome Laboratory, DARPA. Office of Naval Research

Project Staff

Steven G. Patterson, Erwin Lau, Kevin Pipe, Gale Petrich, Professor Leslie Kolodziejski, Professor Rajeev J. Ram

Bipolar cascade lasers (BCLs) are capable of demonstrating voltage, incremental resistance, and differential slope efficiencies that are ideally the sum of the individual laser junctions in the cascade. The first room temperature (RT), continuous wave (CW) performance of a BCL was recently reported with a demonstrated differential slope efficiency of 99.3%. The BCL ideally operates by having each injected electron participate in a recombination event in the topmost active region, then tunnel from the valence band of the first active region into the conduction band of the next active region, participate in another recombination event, and so on through each stage of the cascade. A cascade of N sections then requires a voltage bias of N diode voltage drops. Since the threshold current of each active region is ideally the same as a single stage laser, the DC power dissipation, and hence the heating, of the BCL also goes up linearly with the number of cascaded sections. It can then be expected that this increased heating will effect the thermal properties of the BCL. The temperature behavior of gain-guided, Fabry-Perot, RT, CW bipolar cascade lasers has been investigated and characterized. The temperature T_o characterizes the sensitivity of the laser's threshold current to temperature, while the temperature T_1 characterizes the sensitivity of the laser's differential slope efficiency to temperature. Thermal characterization also gives insight into device functioning and points the way toward better laser design.

The devices used in the thermal study for this paper are 300 μm long devices with a single high-reflectivity (HR) coated facet (R = 95%). All devices have Fabry-Perot cavities and are gain-guided. The lasing wavelength of both QWs is ~ 990 nm. Shown in Figure 6 is the temperature dependence of the light power vs. injected current for a representative 20 μm wide HR-coated device. In Figure 7a it can be seen, that for the BCL devices being studied here, the continuous-wave T_o = 102.5 K over the heatsink temperature range of 10-40 ^oC, but drops off dramatically to 55.7 K for heatsink temperatures in the range of 50-80 ^oC. Over the entire temperature range of operation T_o = 76 K. Two values for T_1 can be extracted for the BCL, corresponding to the temperature dependence of the differential slope efficiency both below and above the onset of lasing in the bottom active region in the L-I slope. For the 20 μm wide HR coated device, the values of T_1 are 81 K (below the second active region's threshold) and 47 K (above the second active region's threshold) (Fig. 7b). It is seen that T_1 drops most dramatically above heatsink temperatures of 40-50 ^oC.

The top surface temperatures of the BCL and a conventional single QW InGaP/GaAs/InGaAs laser were measured as a function of bias current density. The length of the conventional laser was chosen so as to have similar mirror losses as the BCL. Measurements were made by directly touching a calibrated micro-thermocouple to the metal biasing contacts. The bottom-side heatsink temperature was maintained at 20 ^oC with the laser submount thermally connected to the heatsink via thermally conductive silicone paste. The BCL heats over twice as quickly as the conventional single QW device. Secondary evidence of the increased temperature of the QW is found by comparing the slope efficiency of the single QW conventional laser with the slope efficiency of the BCL. The conventional device has a slope efficiency of 60%, while the BCL's 93% efficiency is well below the expected 120% efficiency.

Finite element modeling of both the BCL and the conventional, single stage InGaP/InGaAs/GaAs laser was performed. The solid lines in Figure 8 show the surface temperature values as determined by simulation. Very good agreement between simulation and measurement can be seen, indicating the simulations can provide insight into the temperature distribution within the devices. The most important result illuminated by the simulation is the realization that even when the voltage of the lasing (top) active region is clamped, the unclamped (non-lasing) bottom active region continues to act as a significant source of heating for the top active region. The top active region also acts as a heat source for the bottom active region, further delaying onset of lasing for the bottom active region. By the time the bottom active region reaches threshold, the thermally increased optical losses have compromised the differential slope efficiency of the BCL.

The dashed lines in Figure 8 are the active region temperatures calculated using the thermal impedance. There is excellent agreement between the calculation based upon Z_T and the

measurements of the surface temperature for the conventional device. For the BCL agreement is good for bias current densities less than 800 A/cm^2, but divergent behavior is exhibited beyond the onset of lasing in the top active region. Utilizing the information obtained in this study, a second generation BCL has been designed to include multiple quantum-well active regions, broadened waveguides, current blocking apertures, and a reduced-bandgap tunnel junction.

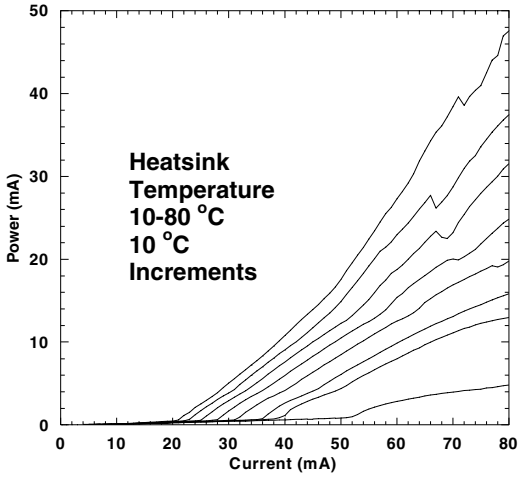

Fig. 6. Light power vs. input current for a 20 μm wide, 300 μm long, RT, CW, Fabry-Perot gain-guided, single facet HR coated BCL. CW lasing is achieved up to 80 °C. Dots indicate onset of lasing for the bottom active region. Inset: The bipolar cascade device structure.

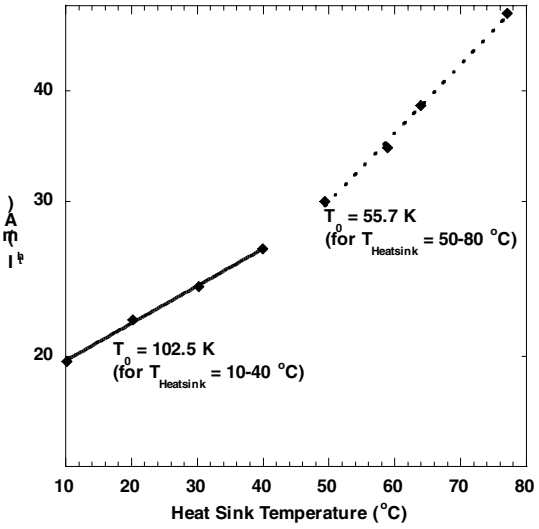

Fig 7a. CW threshold current versus heatsink temperature for the same device as Fig.6. T_o is 104.5 K over the range 10-40 °C, but abruptly drops to 55.7 K for heatsink temperatures in the range 50-80 °C.

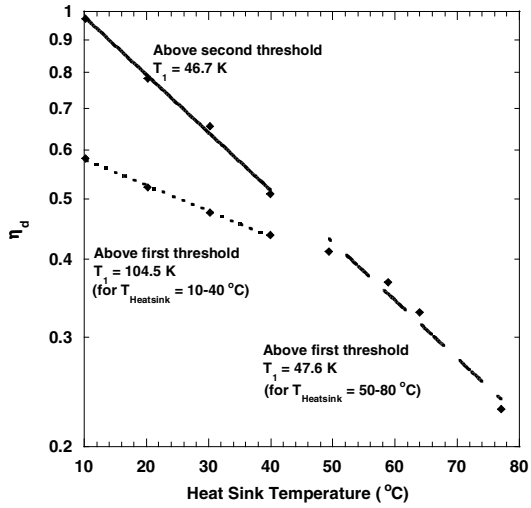

Fig. 7b. T_1 values for the device of Fig. 6.

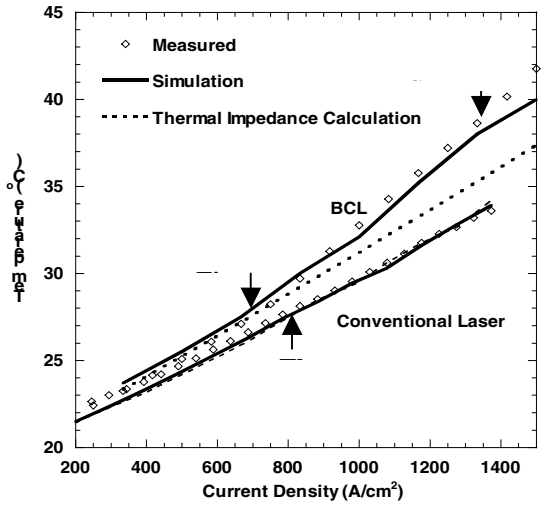

Fig 8. Surface temperature measurements and simulations for a BCL and a single QW conventional laser vs. bias current.

6 Dynamics and Noise in Intersubband Lasers

Sponsor

Office of Naval Research

Project Staff

Farhan Rana, Professor Rajeev J. Ram

Unipolar quantum cascade lasers (QCLs) utilizing intersubband transitions to generate photons have become important sources of light in the mid-infrared region (5 - 15 μm). The recent advances in new materials systems, like the nitrides and the antimonides, open the possibility of QCLs operating at wavelengths close to 1.55 μm, which is an important wavelength region for optical communication systems. Despite the significant progress made in the experimental realization of QCLs, no papers have appeared in the literature which quantitatively describe the dynamics of electrons and photons in these lasers, or shed light on the noise properties of these lasers. We have developed a comprehensive theoretical model that achieves these goals.

Fig. 9 shows a multiple quantum well structure that defines a single stage of a QCL. QCLs are different from interband semiconductor lasers in three important ways which can have a significant impact on their noise properties. First, electron transport in QCLs takes place by tunneling between states in adjacent quantum wells. It is well known that coulomb interactions in resonant tunneling in quantum well structures can suppress (or enhance) current noise by providing a negative (or positive) feedback. High impedance suppression of current noise in interband semiconductor lasers can lead to squeezed photon output. It is therefore intriguing whether coulomb correlations in electron transport can also lead to squeezing in QCLs. Any model for the photon noise in QCLs must take into account these coulomb correlations self-consistently. Secondly, in interband semiconductor lasers the carrier density does not increase beyond its threshold value and, therefore, the noise associated with the non-radiative recombination and generation processes also remains unchanged beyond threshold. In QCLs the electron densities in the upper and lower lasing states are not clamped but keep increasing when bias current is increased beyond threshold. As a result non-radiative recombination and generation processes contribute significantly to photon noise even at high current biases. Lastly, since all gain sections in a QCL are connected electrically and optically, electron density fluctuations and photon emission events in different gain sections become correlated. The effect of these correlations on the photon noise spectral density must also be taken into account.

The model developed by us consists of a set of coupled self-consistent Langevin rate equations for fluctuations in electron density in different energy levels of each gain stage. Fluctuations in the electron density are caused by radiative and non-radiative scattering processes, electron tunneling processes and also by fluctuations in the current injected into the gain stage. Fluctuations in the current are a relaxational response to electron scattering and tunneling events occurring inside all the gain stages of the QCL, and they are also caused by sources external to the laser which include thermal noise sources associated with circuit resistances. Photon density fluctuations are also modeled by Langevin rate equations. Electron density fluctuations in different gain stages are all coupled to the photon density fluctuations and to the fluctuations in the current which flows through all the gain stages connected in series. The system of equations obtained this way can easily be solved analytically or numerically to give the current modulation response of the laser and also the spectral density of photon number fluctuations and current fluctuations. Our theoretical model can be used to study a variety of QCLs that have been reported in literature.

Fig. 10 shows the current modulation response of a QCL. The modulation response is overdamped and rolls off around 20 GHz. The modulation bandwidth of most QCLs is primarily limited by the long photon lifetime inside the laser cavity. Fig. 11 shows the Fano Factor for the

current fluctuations as a function of the current bias when the QCL is connected with an ideal voltage source. The suppression of the current fluctuations below the shot noise level is a result of the coulomb correlations in electron transport, and the fact that the impedance of a single gain stage of a QCL is much smaller than the impedance of the entire QCL. Fig. 12 shows the Relative Intensity Noise (RIN) of a QCL as a function of the bias current. Even though the fluctuations in the pump current are suppressed below the shot noise level, the RIN shows that the photon noise remains above the shot noise level (standard quantum limit), and only at very large bias currents a small (0.2 dB) amount of squeezing is possible. The absence of any significant squeezing in QCLs is due to the fact that the electron densities in the lasing levels do not get clamped but keep increasing with the bias current beyond threshold. And, therefore, contribution to the photon noise from the non-radiative scattering processes also keeps increasing with the bias current.

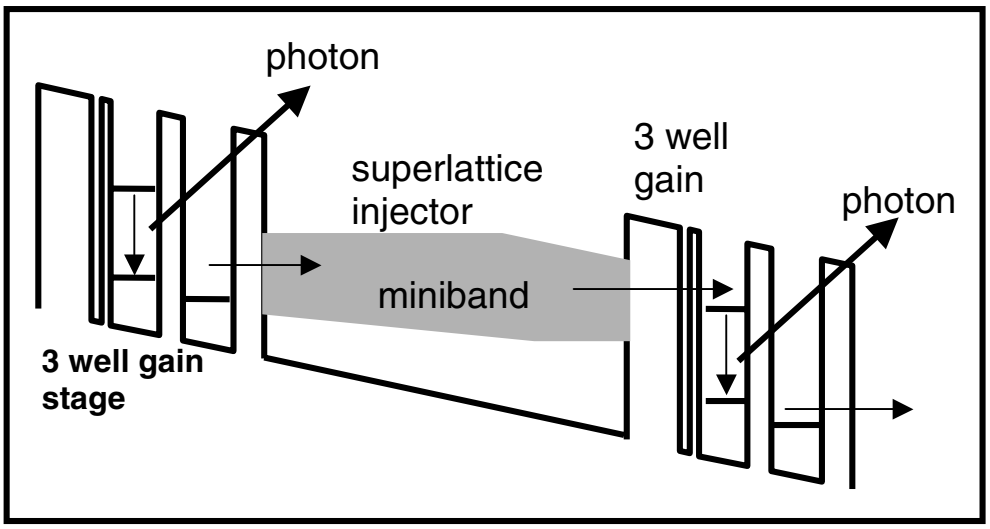

Fig. 9: Gain Stage of a Quantum Cascade Laser

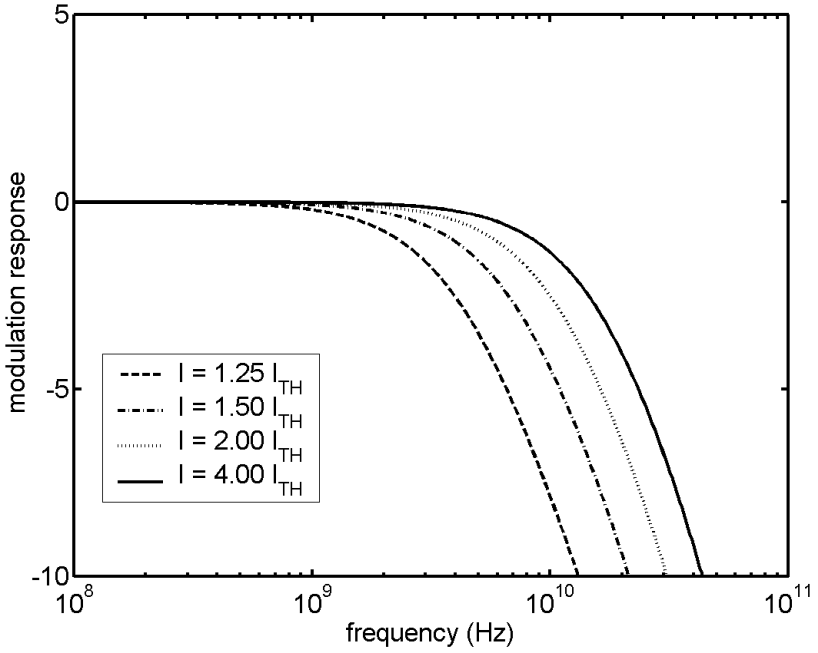

Fig. 10: Current Modulation Response of a Quantum Cascade Laser

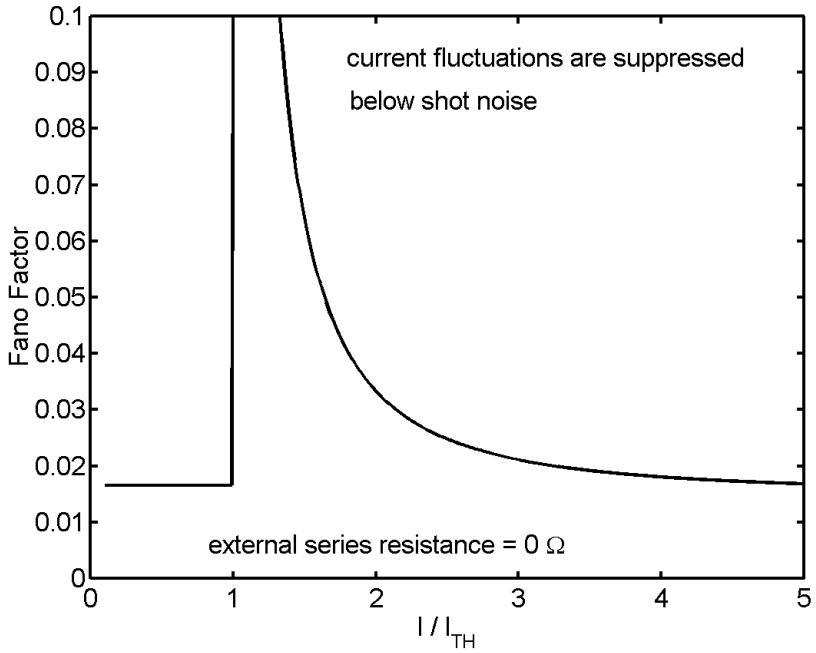

Fig. 11: Fano Factor for Current Fluctuations for a Quantum Cascade Laser

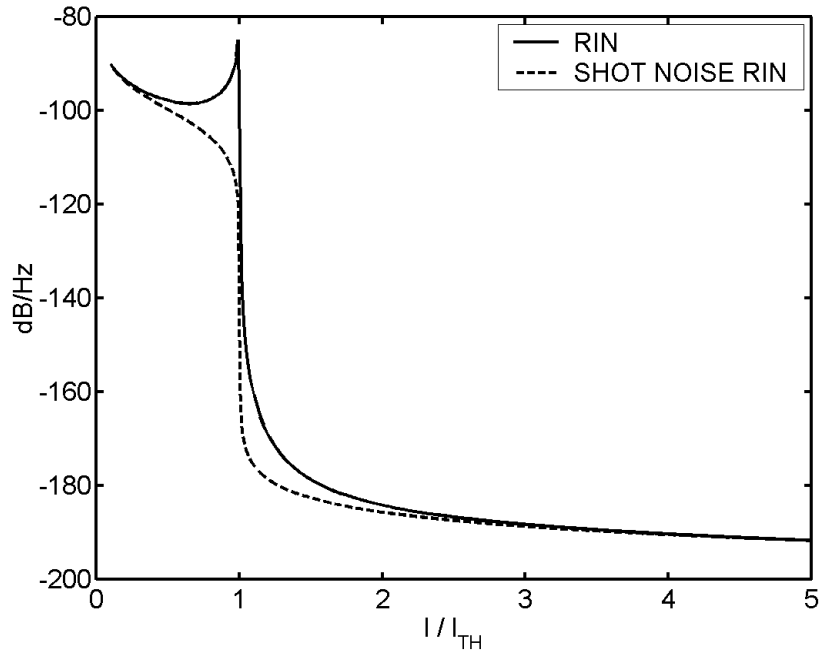

Fig. 12: Relative Intensity Noise (RIN) of a Quantum Cascade Laser

7 Injection Current Internally Cooled Light Emitters (ICICLE)

Sponsor

Office of Naval Research

Project Staff

Kevin P. Pipe, Professor Rajeev J. Ram

Temperature effects are important in semiconductor lasers because heat increases both the spread of the carrier energy distribution and the leakage current out of the quantum wells, making it harder to achieve inversion. In the case of long-wavelength lasers, which suffer from additional optical absorption and Auger recombination, heat management is especially crucial. While mid-infrared lasers have many applications in fields such as pollution monitoring, room-temperature continuous-wave devices do not exist, primarily due to heating problems.

Conventional methods for cooling a laser involve an external structure such as a bonded Peltier cooler; these tend to be bulky and heavy, and are a limiting factor in the downscaling of the device package. The design of the Injection Current Internally Cooled Light Emitter attempts to provide cooling on a small scale by making the cooling mechanism internal to the laser structure. In this novel approach, the same carriers used to produce light also take heat energy out of the lattice.

The band structures for both a conventional laser and for an idealized ICICLE are shown in Figure 13. Whereas carriers in the conventional structure are accelerated by the electric field at the core/cladding interface (and come back into equilibrium by depositing heat in the lattice), carriers in the ICICLE design see a potential barrier. Cooling is achieved through the process of thermionic emission, which is analogous to evaporative cooling.

One material system in which the ICICLE structure can be physically realized is InGaAsSb. These alloys have an inherent type-II interface which allows one to construct the “staircase” ICICLE band structure without resorting to heavy doping. Through the use of electrical and optical simulation software, a mid-IR ICICLE design has emerged. Experimental verification of the design is underway in collaboration with Lincoln Laboratory, which has expertise in the area of antimonide lasers and facilities for their growth.

One key to experimental characterization of the ICICLE structure is temperature measurement. In order to determine the temperature of laser structures, a microthermocouple apparatus has been constructed which is able to detect changes in temperature of 10 mK on a spatial scale of 25 um. The setup has been used to characterize several conventional laser structures, and the measurements have been correlated with theoretical models.

Theoretical work is also being carried out to gain a better understanding of heating and cooling effects in semiconductor lasers. Through a collaboration with UC Santa Cruz, a more complete picture of the dynamics of the ICICLE is being developed. Additional computer simulations, such as 2D heat flow and Monte Carlo, have been created to aid in device modeling.

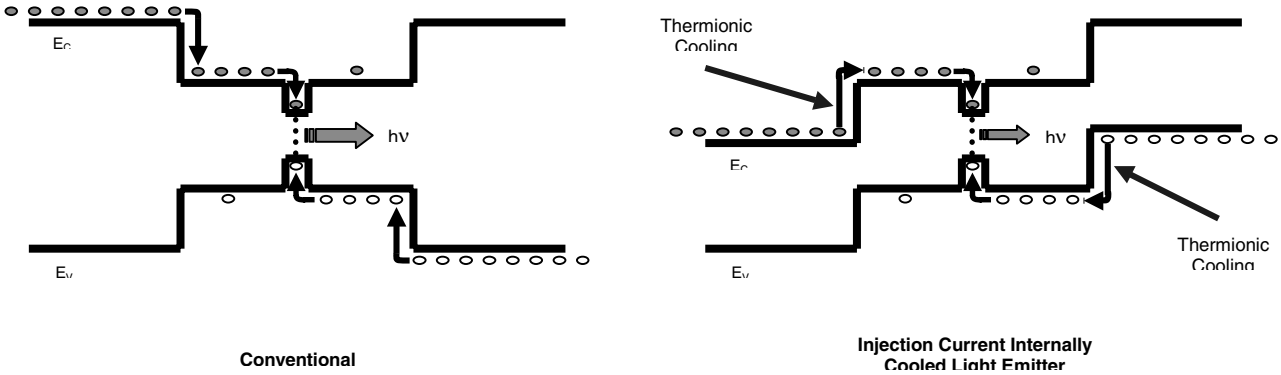

Fig. 13. Band structures for conventional laser and for an idealized ICICLE.

8 Electron Spin Dynamics in Semiconductors

Sponsor

National Science Foundation

Project Staff

Mehmet Yanik, Professor Rajeev J. Ram

The study of spin dynamics is becoming important because of the emerging field of spintronics which aims at using the electron's spin to store, manipulate and transport information. Because of the fundamental nature of spin dependent processes, the study of spin dynamics might also lead to a better understanding of other dynamic quantum processes in interacting systems. For semiconductors optical methods make it possible to filter electron spin dynamics despite the background of other magnetic processes (eg. scattering with holes, magnetic impurities). Spin polarized carriers can be excited to the conduction band from the valence bands, and the evolution of the collective electron spin polarization can be monitored. We are interested in understanding the major spin scattering mechanisms and their dependence on impurity and electron concentration, temperature, interface, magnetic field, spin orbit coupling and particle interactions.

For this purpose, we built the pump probe setup shown in Figure 15 to probe femto second and pico second electron spin dynamics in III-V semiconductors. A tunable Ti/Sapphire laser provides 100 fs -1 ps pulses with repetition rate of 80 MHz. Pulses are split into two by a beam splitter having ultrafast response time and pump pulse passes through a computer controlled translation stage to introduce delay with a spatial resolution of 0.5μm corresponding to 2 fs temporal resolution. The probe pulse passes through a manual translation stage with a spatial resolution of 1μm. Both pulses are polarized by quarter wave plates having ultrafast response times. The Ti/Sapphire laser has noise components up to 9 Mhz due to oscillations in its Argon ion pump source. Pump pulses are chopped by an anti reflection coated acousto-optical modulator at 10 Mhz in order to prevent the intrinsic laser noise. Due to the heating effects at the sample, low frequency noise below 1 kHz is mixes with the probe signal. In order to cancel this noise, the probe pulse is chopped by a low frequency mechanical chopper. The pump and probe pulses are incident onto the sample surface at slightly different angles and the probe beam after being filtered by a circular and a linear polarizer is coupled via a fiber optic link to a low noise photo detector with 125Mhz response bandwidth. Phase-locked detection of detector signals is done at 10Mhz minus 1kHz. Computer control of translation stage and measurement of average laser power with a fast scan and many averaging is used to suppress noise due to laser drift.

Figure 14 plot shows measurements on 80nm n-doped $In_{0.05}GaAs/GaAs$ quantum well with different pump and probe polarizations. From the difference in the decay rate of probe transmission, the carrier recombination and spin dephasing lifetimes are obtained as 0.9ns and 20ps which is in agreement with the literature verifying the pump-probe setup's calibration. Due to interface effects, in heterostructures the spin lifetime is much shorter than in bulk and much longer spin lifetimes in bulk GaAs are expected. Spin lifetime measurements are performed by many groups in various semiconductor systems, however spin dephasing mechanisms in general are not well understood due to various competing processes. Our goal is to understand these mechanisms.

The aim is to develop theoretical models of carrier spin dynamics and assess the effectiveness of various processes by comparing computational results with our experiments. We have performed Monte Carlo (MC) simulations of electron spin dynamics by including processes due to band structure, impurity and phonon scattering. Our calculations are in agreement with previous experiments showing that momentum scattering processes are suppressing spin dephasing due to motional narrowing. However calculated spin lifetimes and the temperature dependencies are much different in magnitude than experimentally observed, suggesting that another mechanism must be involved in suppressing spin dephasing. Electron-electron scattering neglected in the literature due to the difficulty in its treatment might be responsible from the suppression of spin dephasing. We are currently developing models and algorithms to treat non-equilibrium electron-electron scattering processes with arbitrary carrier distribution. Pauli exclusion, screening and exchange scattering processes for arbitrary spin density matrixes are incorporated into MC. The effect of coherent electron-electron exchange scattering on spin polarization is also included as a self-consistent spin dependent potential field.

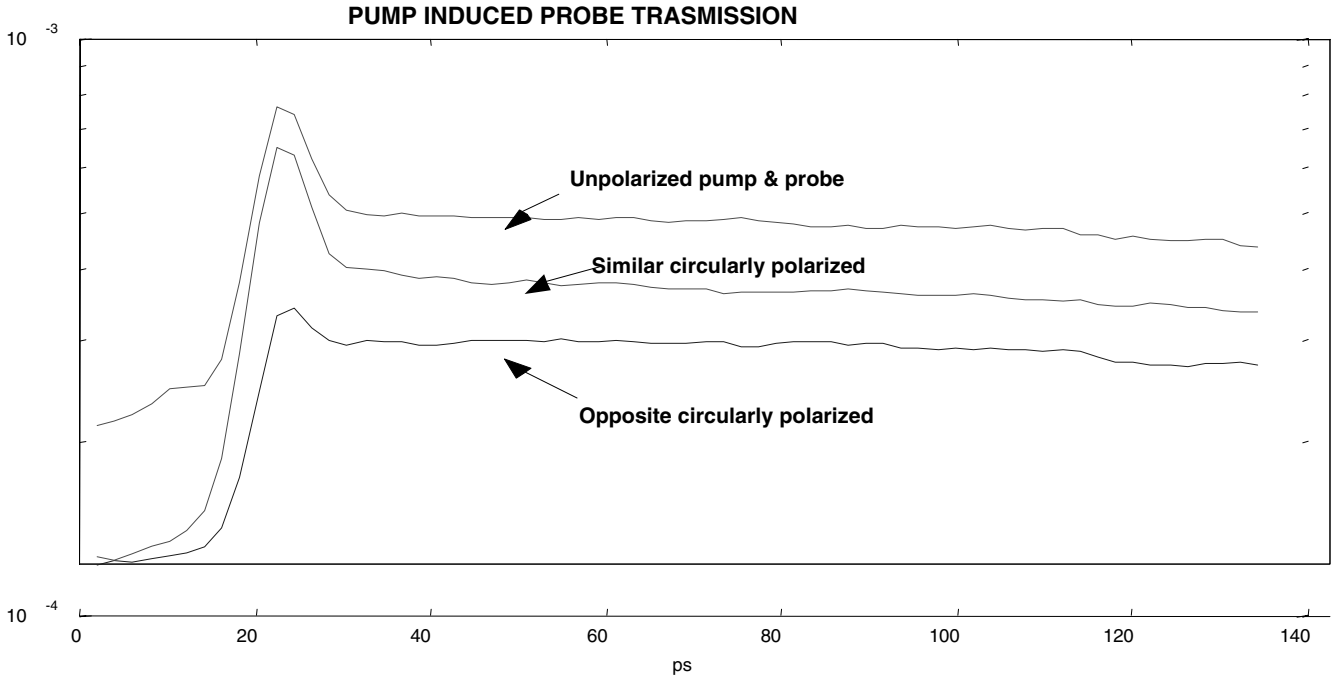

Fig. 14. Measurements on 80nm n-doped $In_{0.05}GaAs/GaAs$ quantum well with different pump and probe polarizations.

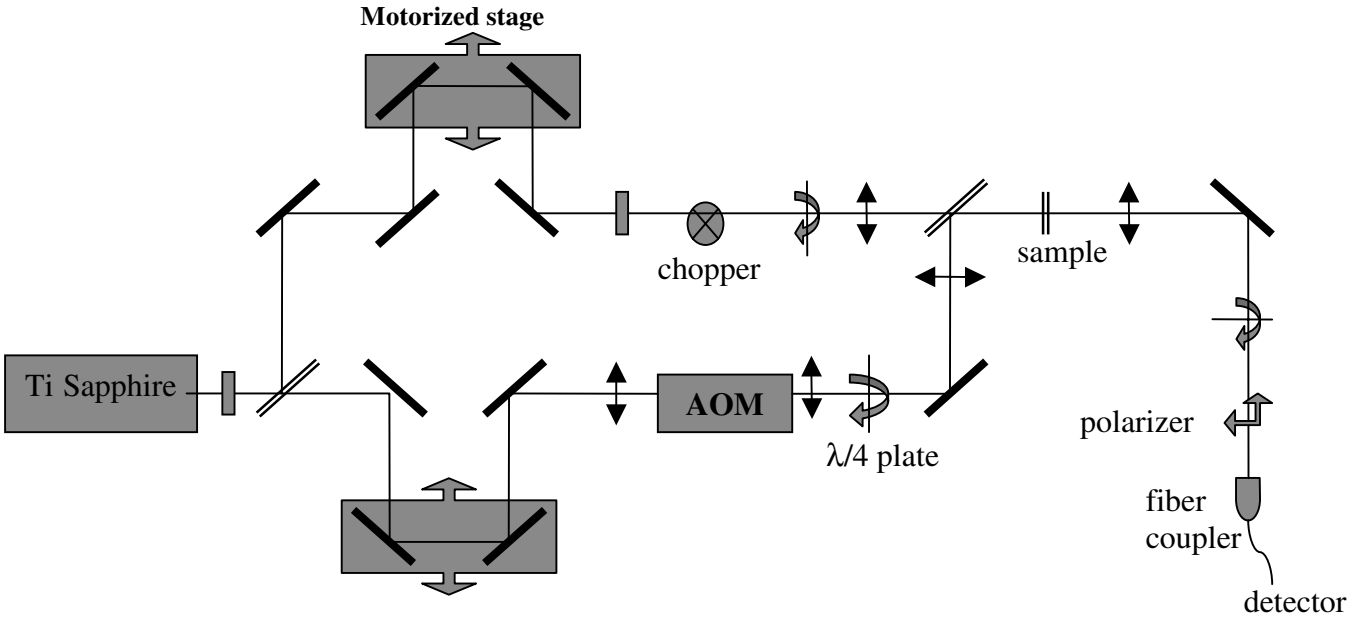

Fig. 15. A pump probe setup built to probe femto second and pico second electron spin dynamics in III-V semiconductors.

8 Magnetic Force Microscopy of Nanomagnetic Arrays

Sponsor

National Science Foundation

Project Staff

Mathew C. Abraham, Dr. Holger Schmidt, Minha Hwang, Timothy Savas, Professor Caroline Ross, Professor Henry I. Smith, Professor Rajeev J. Ram

We studied 100nm period nanomagnetic arrays made by achromatic interferometric lithography combined with electrodeposition[1]. The samples were large (2cm^2), and therefore enabled us to correlate the collective behavior of the arrays measured by bulk Velocity Sensitive Magnetometry (VSM), with the behavior of individual particles measured with magnetic force microscopy (MFM). In this work, we were able to detect direct evidence for the existence of interactions between posts, as well as the influence of these interactions on the bulk magnetization of these samples.

Two samples were studied; both of which have Ni pillars with aspect ratios of approximately 2. Sample-I has pillars with diameter 57nm and height 115nm, while sample-II has diameter of 70nm and height 150nm. Sample-II being more densely packed and having larger particles, as expected, turned out have significantly larger interparticle interaction than Sample-I. This was first inferred by comparing the squareness in the bulk VSM hysteresis loop measurements shown in Fig. 16(a) and (b)[2], and more directly observed with MFM measurements.

In all the MFM measurements presented, the magnetization of the tip is directed perpendicular and into the plane of the sample being imaged. Thus, regions in the sample having magnetization components out of the plane of the sample produced regions of bright contrast and vice-versa. The tips used were made of etched silicon with a tip radius of approximately 30nm and a sputtered 20nm layer of CoCr (Digital Instruments model MESP-LM). The stray magnetic field produced by the tip ≅ 200Oe, was chosen to be significantly less than the average coercive field of the nanomagnets.

Figure 17(a) and Figure 17(d) are MFM images of sample-I in zero magnetization states. The images reveal that the magnetization of the nanomagnets are perpendicular to the plane of the sample. Also, since the spatial resolution of the MFM is ~30nm and the response of the cantilever is relatively uniform over the surface of the nanomagnets, indicates that the magnets are single domain. Figure 17(a) is a "coerced" state obtained by first saturating the sample with a large external magnetic field in the direction out of the plane of the sample and then zeroing out the magnetization by applying a magnetic field in the opposite direction - this state is marked as point X in Figure 16 (a). Figure 17(d) is the AC demagnetized state of sample-I. Figures 2(b) and 2(e) are discretized images of Figure 17(a) and Figure 17(d). And figures 17(c) and 17(f) are autocorelations of Figures 17(b) and 17(e) respectively. Unlike Figure 17(c), Figure 17(f) shows a clear checkerboard type signature indicating that sample is in its "ground state" where the interaction energies between the magnets are minimized. Figure 17(g) is an MFM image of a remnant state of Sample-II. Since there was a significant distribution in the sizes of the nanomagnets, clear MFM images for sample-II were difficult to obtain. Inspite of the unevenness of the sample, on discretizing the image (Figure 17(h)) and performing an autocorelation (Figure 17(i)), we find a clear checkerboard pattern similar to Figure 17(f). The checkerboard pattern is a macroscopic manifestation of the interactions between individual nanomagnets reminiscent of an anti-ferromagnetic ground state. The fact that the spontaneously occurring remnant state of Sample-II shows a strong checkerboard signature as opposed to sample-I which has to be AC demagnetized to display the same is a clear indication that interparticle interactions are significantly greater in sample-II as compared to sample-I.

In addition we were able to make MFM measurements in an adjustable external magnetic field. This provided a hysteresis loop for individual nanomagnets and an ability to compare micro and bulk hysteresis measurements. Also, by analyzing sequences of images taken at incrementally larger external magnetic field, it was possible to observe the influence of the magnetic state of neighboring posts on the switching field of individual posts.

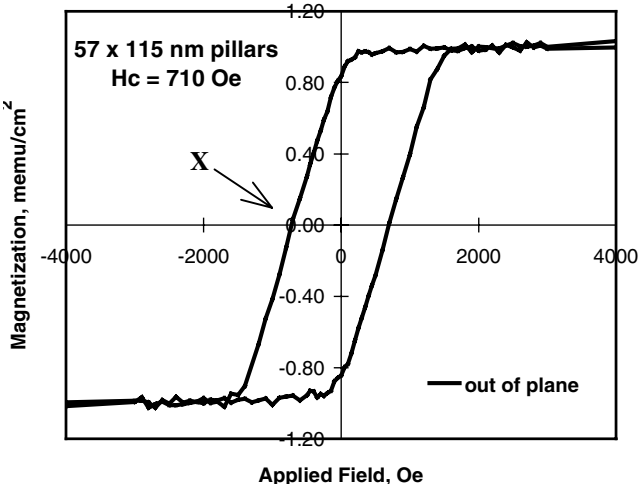

Figure 16a) Out of plane magnetization hysteresis loop of Sample-I. Point X is the coerced state studied using MFM – see Figure 2.

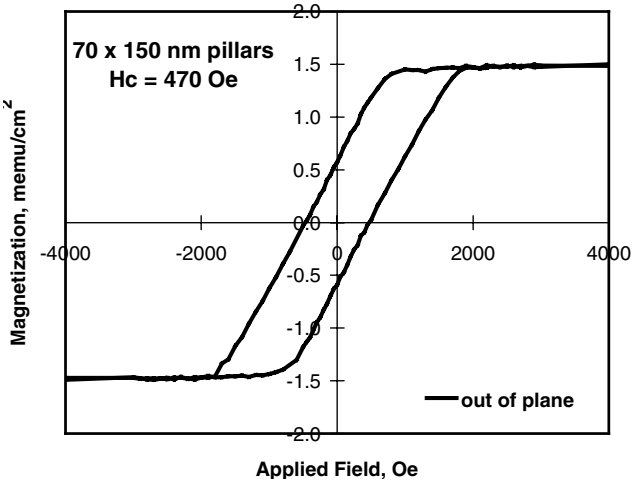

Figure 16b) Out of plane magnetization hysteresis loop of Sample-II.

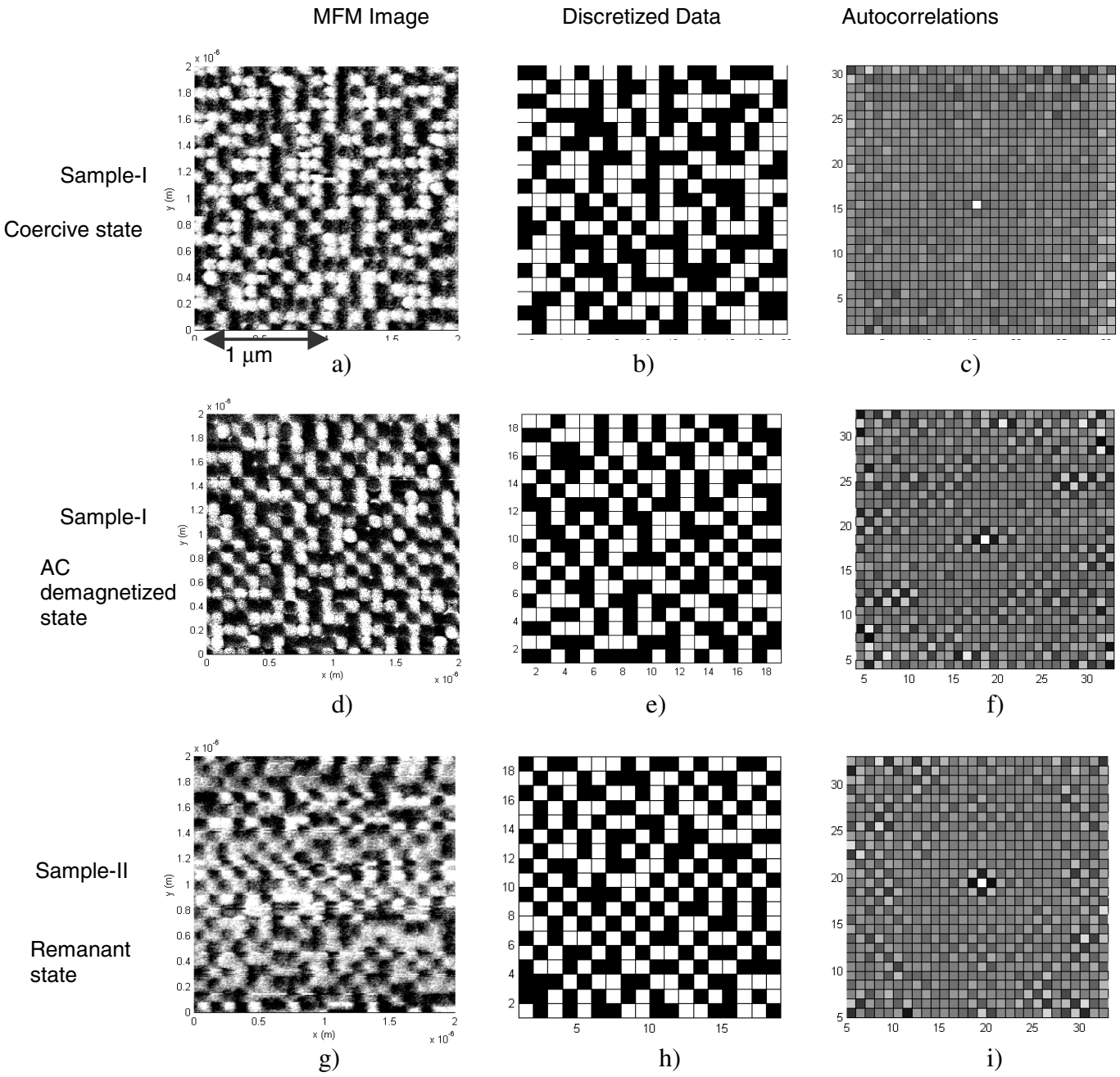

Fig 17. a), d), g) are MFM images, b),e),h) are the corresponding discretized data, and c), f) and i) are the autocorrelations of b), e) and h). The coercive state of Sample-I shows no indication of interparticle interactions as compared to the AC demagnetized state of Sample-I and the remanant state of Sample-II which both show regions of checkerboard pattern that correspond to the magnetostatic ground state of the sample .